photonics

Article

A Silica Capillary-Based Sensor with Access Channels for the Simultaneous Measurement of Pressure and Temperature

João P. Santos [1], Jörg Bierlich [2], Jens Kobelke [2] and Marta S. Ferreira [1,*]

[1] i3N & Department of Physics, University of Aveiro, Campus Universitario de Santiago, 3810-193 Aveiro, Portugal; jpfsantos@ua.pt
[2] Leibniz Institute of Photonic Technology, Albert-Einstein-Straße 9, 07745 Jena, Germany; joerg.bierlich@leibniz-ipht.de (J.B.); jens.kobelke@leibniz-ipht.de (J.K.)
* Correspondence: marta.ferreira@ua.pt; Tel.: +351-234-370-899

Abstract: A hybrid fiber sensor for the simultaneous measurement of pressure and temperature is proposed. The sensor is constituted of a section of silica capillary tube (SCT) whereat access channels are created with two different methods: instilling a bubble on the fiber by employing successive arc discharges on the SCT whilst under pressure and splicing the SCT with another section of SCT with a smaller inner diameter. The reflection-based sensor enhances Fabry–Perot interference (FPI) and antiresonant (AR) guidance, simultaneously, in a single sensing element of a few millimeters. A comparison study between the access channel methods reveals higher spectral visibility for the bubble method and similar pressure and temperature resolutions. For a 2.58 mm long sensor with a bubble, the sensitivity to pressure is 4.09 ± 0.01 nm/MPa and -3.7 ± 0.1 nm/MPa for the FPI and AR, respectively, while its sensitivity to temperature is -0.20 ± 0.02 pm/°C and 24.0 ± 0.5 pm/°C, respectively, for the FPI and AR, which are within the numerically calculated sensitivities. The sensor is robust and has a convenient reflective probe with easy and low-cost fabrication, granting high competitiveness in actual applications.

Keywords: optical fiber sensor; silica capillary tube; access channel; bubble; Fabry–Perot interferometer; antiresonant guidance; pressure; temperature

Citation: Santos, J.P.; Bierlich, J.; Kobelke, J.; Ferreira, M.S. A Silica Capillary-Based Sensor with Access Channels for the Simultaneous Measurement of Pressure and Temperature. *Photonics* **2023**, *10*, 1029. https://doi.org/10.3390/photonics10091029

Received: 31 July 2023
Revised: 5 September 2023
Accepted: 6 September 2023
Published: 8 September 2023

1. Introduction

Gas pressure sensing is a high-demand application of optical fiber sensors in the industrial and environmental monitoring fields [1,2]. There has been an increase in interest in their research due to the devices' compact size, high sensitivity, and electromagnetic interference immunity [3].

Different configurations have been employed for pressure sensing applications, including fiber gratings and interferometers like Mach–Zehnder (MZI), Sagnac (SI), and Fabry–Perot (FPI). Pressure sensors based on fiber gratings generally present low sensitivities [4], while MZI- [5] and SI-based [6] sensors require complex manufacturing operations. The mechanism of a diaphragm-based pressure sensor is based on variations of the cavity length, whereas for open cavities, it relies on variations of the refractive index (RI). Fiber-tip FPIs based on diaphragms possess limited durability and operation stability due to the creep behavior of the thin diaphragm structure [2], only operating in limited gas-pressure ranges [7]. The mechanical deformations of the diaphragm hinder the general linearity, repeatability, and resilience of the sensors [7]. Therefore, a diaphragm-free pressure sensor is desirable.

Sensors based on open cavities, which are therefore diaphragm-free, have been developed, including FPI-based [7,8] and antiresonant (AR)-based [1,3] sensors. These pressure sensors have extended measurement ranges owing to their different principle of operation, which is rooted in the relationship between the gas pressure and the RI variation [8].

Nevertheless, this principle is also affected by temperature, decreasing the gas-pressure sensitivity of FPI- and AR-based sensors with increasing temperatures. Therefore, temperature compensation is required when measuring gas pressure [2].

The miniaturization of optical sensors has also brought about photonic integrated circuits, more specifically, micro-ring resonators. This technology has showcased a very high sensitivity to pressure and temperature: 2.77 nm/GPa in a pressure range of 0–10 GPa [9] and 49.77 nm/MPa in a range of 3–9 MPa [10], and 2.9 nm/°C in a range of 0–50 °C [11]. Their low power requirements and fast response to environmental changes places them as highly competitive sensing technologies. However, they have complex fabrication processes, with a relatively high cost, delicate nature, and challenging optical alignment and provide inaccurate measurements for extreme pressure and temperature.

To compensate for cross-sensitivity issues verified in conventional optical fiber sensors, another cascaded sensor can be added, increasing the system complexity and total sensing length. Alternatively, by adopting a hybrid sensor where, in a single structure, the independent and simultaneous measurement of multiple parameters can be made, the fiber sensor thus presents a simpler configuration, working principle, and fabrication technique, overall miniaturizing the sensor [12].

Hybrid sensors have been investigated for multi-parameter measurements using cascaded fiber Bragg gratings and dual-cavity FPIs [3,13]. With a sensor based on FPI and AR mechanisms in a sandwich structure made of a single mode fiber (SMF) and a silica capillary tube (SCT–SMF), dual-parameter measurements in a single cavity can be achieved [2].

The microchannels that act as an open cavity for pressure sensing in previous studies have often been fabricated by expensive equipment, such as femtosecond laser micromachining [1,2]. Using this technique, Hou et al. attained a gas-pressure AR-based sensor [1], while Gao et al. achieved a hybrid sensor for self-temperature-calibrated gas-pressure detection [2]. Other techniques include using C-shaped fibers, butt-coupling [14], as well as focused ion beam milling [15]. Furthermore, Yang et al. fabricated open-air cavities with a clever method by fusion splicing an SMF with an SCT [3]. Additionally, He et al. developed a hybrid sensor for pressure and temperature measurements by splicing an SCT between an SMF and another SCT with a smaller inner diameter [16]. A different method for a lateral access hole through the fiber wall in photonic crystal fibers (PCFs) was demonstrated that utilized a fusion splicer and application of pressure, though great deformation was introduced around the hole [17]. As such, it is desired to apply the innovative low-cost side hole method in a capillary-based fiber for pressure detection as it is able to achieve an open cavity without resorting to expensive equipment or cascading another capillary.

In this article, a diaphragm-free hybrid fiber sensor for the simultaneous measurement of pressure and temperature based on an SCT with access channels is proposed. The sensor is composed of a section of SCT spliced between two fibers, creating two interferometers that occur simultaneously: FPI and AR guidance. The access channels were fabricated via two methods, acting as a micro gas inlet. The bubble-based method was found to have higher visibility in the FPI and AR spectra than the thin-core SCT method, while granting the sensor greater versatility. The interferometric phenomena allowed the discrimination of the parameters under study.

2. Operation Principle

The configuration of the proposed hybrid fiber sensor is based on a sandwich structure where a section of an SCT is spliced between two fibers. This SCT was fabricated at the Leibniz Institute of Photonic Technology, in Jena, Germany. Considering an SMF–SCT–SMF configuration, the SCT has an inner diameter, $2r$, of 57 ± 2 μm and an outer diameter of ~125 μm, as seen in Figure 1a. The SCT length and cladding thickness are denoted as L and d, respectively. The RIs of the silica cladding and hollow core are denoted as n_2 and n_0, respectively, while the RIs of the SMF core and cladding are designated as n_1 and n_2, respectively. At 1550 nm, the RIs are approximately $n_0 = 1; n_1 = 1.445; n_2 = 1.444$ [2,18].

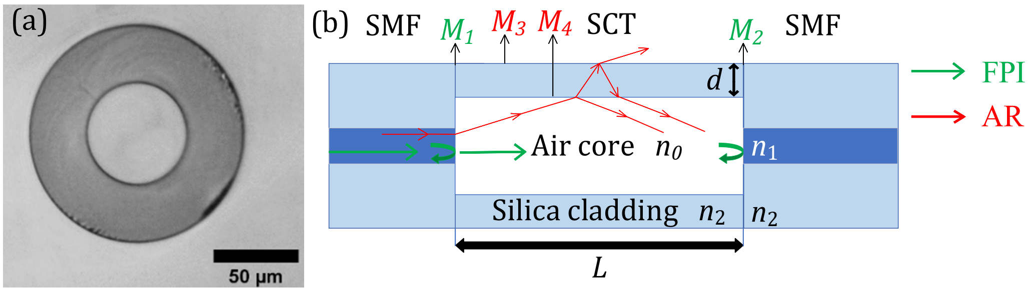

Figure 1. (**a**) Cross-section view of the SCT under a microscope. (**b**) Schematic diagram of multiple reflections that constitute an FPI (green) and interferometry by AR guidance (red) in the SMF–SCF–SMF configuration.

FP interferometry occurs when two high-reflectance parallel surfaces are placed a certain distance, L, from one another, resulting in a multiple reflection mechanism. For the configuration used, the interfaces correspond to the M_1 and M_2 mirrors in the capillary and the FPI is formed along the axial direction. The peak wavelength of the FPI is expressed as [2]:

$$\lambda_{FPI} = \frac{2L}{m} n_0, \tag{1}$$

where m is a positive integer that corresponds to the resonance order. Its free spectral range (FSR) is given by:

$$FSR_{FP} = \frac{\lambda_{m+1}\lambda_m}{2Ln_0}. \tag{2}$$

For a certain capillary length above a certain critical value, L_c [19], due to a lower RI of the core compared to the cladding RI, the AR reflecting optical waveguide mechanism is verified wherein light is coupled into the cladding, forming an FP cavity defined by the M_3 and M_4 interfaces along the radial direction [20]. For the AR wavelengths, i.e., wavelengths that do not satisfy the resonant condition, destructive interference occurs, and light will be reflected within the resonator, refracted back and fully confined in the capillary core. However, for resonant wavelengths, constructive interference will take place, meaning that the FP resonator is highly transparent for these wavelengths and light does not reflect in the air–silica interface. Instead, it will escape the resonator and leak out from the cladding to the outside of the fiber, as shown in Figure 1b, resulting in a low transmission intensity part of the spectrum [21].

The lossy dip occurs when the wavelength meets the resonant condition of the cladding, expressed as [1]:

$$\lambda_{AR} = \frac{2d}{m}\sqrt{n_2^2 - n_0^2}, \tag{3}$$

where m is the resonance order. Its FSR is given by:

$$FSR_{AR} = \frac{\lambda_{m+1}\lambda_m}{2d\sqrt{n_2^2 - n_0^2}}. \tag{4}$$

The FPI pressure sensitivity can be derived from (1) as:

$$\frac{\partial \lambda_{FPI}}{\partial P} = \left(\frac{1}{n_0}\frac{\partial n_0}{\partial P} + \frac{1}{L}\frac{\partial L}{\partial P}\right)\lambda_{FPI}. \tag{5}$$

The pressure sensitivity of the AR component of this sensor is an accumulation of three factor contributions: (i) the RI variation in the hollow core, S_{air}, (ii) the structural deformation of the silica cladding, $S_{structure}$, and (iii) the RI change of the silica cladding as a result of the deformation in (ii) due to the strain-optic effect, S_{silica}. The AR pressure sensitivity, derived from (3), is given by:

$$\frac{\partial\lambda_{AR}}{\partial P} = S_{air} + S_{structure} + S_{silica} = \left(-\frac{n_0}{n_2^2 - n_0^2}\frac{\partial n_0}{\partial P} + \frac{1}{d}\frac{\partial d}{\partial P} + \frac{n_2}{n_2^2 - n_0^2}\frac{\partial n_2}{\partial P}\right)\lambda_{AR}. \quad (6)$$

The RI of air depends on pressure (P) and temperature (T) according to Édlen's equation as a first approximation [1]:

$$n_0 = 1 + \frac{2.8793 \times 10^{-9} \times P}{1 + 0.003661 \times T}. \quad (7)$$

Therefore, an increase in pressure results in an increase in n_0. Considering $\lambda_{FPI} \approx 1550$ nm and a temperature of 25 °C, the first term of (5) results in a sensitivity of the FPI of 4.089 nm/MPa. Similarly, the value of S_{air}, considering $\lambda_{AR} \approx 1555$ nm, was obtained as -3.78 nm/MPa.

Concerning the values of $S_{structure}$ and S_{silica}, it is required to calculate the structural deformation and strain distributions over the silica cladding. Assuming a single layer model with an inner and outer radius, r_1 and r_2, one can analyze the elasticity of the SCT. Across the cladding region, the stress expression can be written as [1]:

$$\begin{cases} \sigma_r = \frac{A}{r^2} + 2C \\ \sigma_\theta = -\frac{A}{r^2} + 2C \\ \sigma_z = D \end{cases}. \quad (8)$$

where A, C, and D are constants. The strain tensor for the silica cladding can, therefore, be obtained by substituting (8) into the Hooke's law, obtaining [22]:

$$\begin{cases} \varepsilon_r = \frac{1}{E_{Si}}\left[(1+v_{Si})\frac{A}{r^2} + 2C(1-v_{Si}) - v_{Si}D)\right] \\ \varepsilon_\theta = \frac{1}{E_{Si}}\left[-(1+v_{Si})\frac{A}{r^2} + 2C(1-v_{Si}) - v_{Si}D)\right] \\ \varepsilon_z = \frac{1}{E_{Si}}(D - 4v_{Si}C) \end{cases}, \quad (9)$$

where E_{Si} and v_{Si} are Young's modulus and the Poisson's ratio of fused silica, which correspond to 73 GPa and 0.17 arb. un., respectively [23]. Generically, the pressure in the outer cladding corresponds to P_o, while the pressure at the inner cladding is P_i. The boundary conditions are, thereby, given by:

$$\begin{cases} \sigma_{r_1} = P_i \\ \sigma_{r_2} = P_o \\ \pi\sigma_z(r_2^2 - r_1^2) + \pi(P_i r_1^2 - P_o r_2^2) = 0 \end{cases}, \quad (10)$$

where the values of r_1 and r_2 of the SCT used in this work are 34 µm and 62.5 µm, respectively. These conditions are a consequence of the sensor being fixed at both ends, nullifying the effect of the pressure applied from the two ends of the sensor, which results in a minimal pressure-induced longitudinal strain, ε_z [1]. Therefore, the constant values are:

$$\begin{cases} A = \frac{r_1^2 r_2^2 (P_o - P_i)}{r_1^2 - r_2^2} \\ C = \frac{r_1^2 P_i - r_2^2 P_o}{2(r_1^2 - r_2^2)} \\ D = \frac{r_1^2 P_i - r_2^2 P_o}{r_2^2 - r_1^2} \end{cases}. \quad (11)$$

Considering the closed sensor configuration, $P_o = P$ and $P_i = 0$; whereas, for open sensors $P_o = P$ and $P_i = -P$, as depicted in Figure 2. The pressure effect in the hole is not considered for this study.

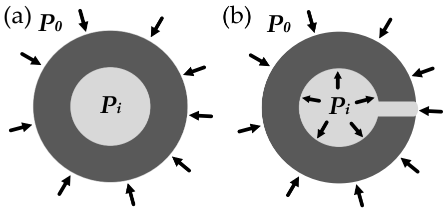

Figure 2. Schematic diagram of a (**a**) closed and (**b**) open sensor.

The stress and strain distributions on the silica cladding can, then, be obtained for both configurations. In Figure 3a, the radial and azimuthal strain distributions for the cladding region, ε_r and ε_θ, respectively, are plotted for an applied pressure of 0.4 MPa. Similarly, in Figure 3b, the radial displacement, $u_r = r \times \varepsilon_\theta$, of the cladding region is plotted for an applied pressure of 0.4 MPa.

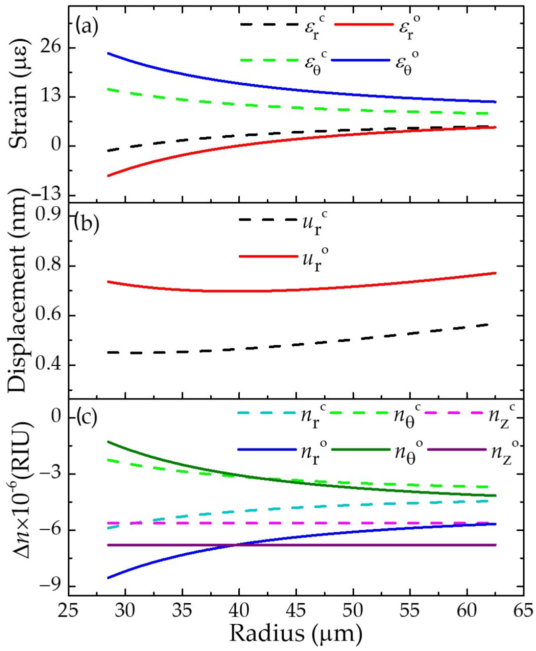

Figure 3. Distribution of (**a**) radial strain and azimuthal strain, (**b**) radial displacement, and (**c**) the RI component of the SCT cladding region for closed and open sensors considering an applied pressure of 0.4 MPa.

Greater strain can be observed in open sensors, although in both configurations, the shift is positive in azimuthal strain and negative in radial strain, increasing towards the inner cladding. The maximum displacement of open sensors is 0.73 nm, while for closed ones, it is 0.54 nm, displaying greater displacement near the outer cladding.

The RI variation that is consequential from the strain-optic effect of the aforementioned displacement can be obtained as:

$$\begin{cases} \Delta n_r = -\frac{1}{2}n_0^3(p_{11}\varepsilon_r + p_{12}\varepsilon_\theta) \\ \Delta n_\theta = -\frac{1}{2}n_0^3(p_{12}\varepsilon_r + p_{11}\varepsilon_\theta), \\ \Delta n_z = -\frac{1}{2}n_0^3(p_{12}\varepsilon_r + p_{12}\varepsilon_\theta) \end{cases} \tag{12}$$

where p_{11} and p_{12} are the strain-optic tensors for fused silica, corresponding to 0.121 and 0.27, respectively [24]. The RI variation given in Figure 3c reveals that the longitudinal component does not vary across the cladding region and that the azimuthal strain pertains to a low shift. The radial RI change is the most significant out of the three components for this configuration, with the highest value at the inner cladding of -8.55×10^{-6} RIU for open sensors and -5.89×10^{-6} RIU for closed sensors.

The final pressure sensitivity of the AR component for an open sensor with one access channel can, finally, be calculated by substituting the acquired values into (6). When the pressure level is raised to 0.4 MPa, considering again that $\lambda_{AR} \approx 1555\ nm$, $S_{structure}$ is ~0.0846 nm/MPa and S_{silica} is approximately -0.0447 nm/MPa. The total value of $\frac{\partial \lambda_{AR}}{\partial P}$ for this configuration is, therefore, approximately -3.74 nm/MPa.

In closed sensors, the core RI will remain constant considering that there is no gas inlet in the fiber, meaning pressure inside the air cavity will not vary. The value of $S_{structure}$ in this configuration is ~0.0621 nm/MPa and the value of S_{silica} is approximately -0.0308 nm/MPa, for a total value of $\frac{\partial \lambda_{AR}}{\partial P}$ of ~0.0313 nm/MPa.

As a response to an applied temperature rise, materials suffer an expansion, given by the thermal expansion coefficient (TEC), and a RI variation, given by the thermo-optic coefficient (TOC). For silica, these coefficients are ~5.56×10^{-7}/°C and ~8.6×10^{-6}/°C, respectively [25]. On the other hand, the FPI cavity is made of air, whose RI practically does not vary with temperature. Therefore, the FPI sensitivity to temperature is expected to be low. Given that in (3), there is a dependence on d and n_2, not only is the AR sensitivity positive, but it is also much greater than the FPI sensitivity.

$$\frac{\partial \lambda_{FPI}}{\partial T} = \left(\frac{1}{n_0} \frac{\partial n_0}{\partial T} + \frac{1}{L} \frac{\partial L}{\partial T} \right) \lambda_{FPI}, \tag{13}$$

$$\frac{\partial \lambda_{AR}}{\partial T} = \left(\alpha + \frac{n_2^2}{n_2^2 - n_0^2} \beta \right) \lambda_{AR}, \tag{14}$$

where α and β are the silica's TEC and TOC, respectively. Considering $\lambda_{FPI} \approx 1550$ nm and $\lambda_{AR} \approx 1555$ nm, values of ~0.86 pm/°C and ~26.7 pm/°C were respectively obtained for FPI and AR.

3. Materials and Methods

Two configurations were developed depending on the access channel method. Generally, a sandwich configuration was employed where a section of the SCT was spliced between two fibers. The splices were performed in the manual mode of the Fujikura FMS-40S fusion splicer with a power of 15 bits (arbitrary unit) and an arc time of 500 ms whilst applying an offset in order not to compromise the capillary. Note that the parameters in the automatic mode are 20 bits and 2000 ms, respectively.

In an effort to grant the sensor responsiveness to pressure, access channels were instilled in the fiber that allow gas entrance through the channel into the structure. This was developed in two distinctive manners.

One method involved splicing the SCT between an SMF (Corning, SMF-28) and another capillary of a different inner diameter, as shown in Figure 4a–d. Hence, the access channel is located on the free end of the second capillary in its hollow core. For clarity, the sensing head will hereafter be denominated as the thick-core SCT, whereas the second capillary will be denoted as the thin-core SCT or simply the capillary, when referring to the access method. The thin-core SCT used for this work has a diameter of ~20 µm. This small inner diameter was chosen so that it does not interfere with the mirror defined by the interface between the SCTs, while being sufficiently large to avoid collapse during fusion splicing. The diameter of the thick-core SCT was chosen as a compromise between the size of the core and the thickness of the cladding. Firstly, the large size of the core aims for greater interactions between the propagating light and the air molecules for pressure detection. Secondly, the thickness of the capillary is also relevant for the excitement of AR guidance [16], thus fulfilling the hybrid role of the sensor.

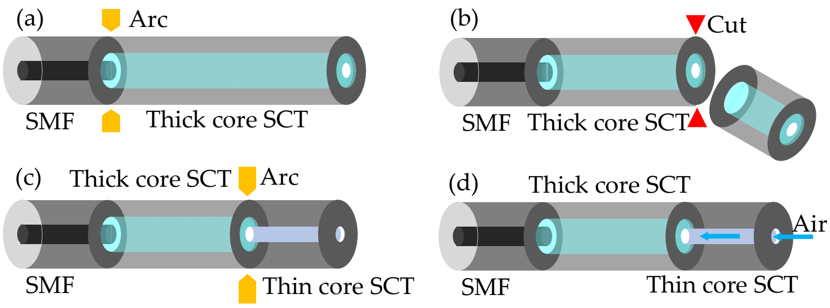

Figure 4. Schematic diagram of the thin-core-SCT-based fiber sensor. (**a**) Splicing the SMF with a thick core SCT. (**b**) Cleaving the desired capillary length. (**c**) Splicing the free end of the thick core SCT with a thin core SCT. (**d**) The access channel is located at the free end of the thin core SCT.

The other method is the instillment of a bubble in the SCT. For this method, the sensing head was spliced between two SMFs, as shown in Figure 5. This bubble is an air cavity that is achieved in the fusion splicer by performing several successive arcs on the capillary whilst under pressure. For this purpose, the parameters used in the manual mode were a power of 20 bits with a first arc of 1300 ms and re-arcs of 700 ms, under a pressure of approximately 270 mbar. These parameters were chosen empirically and established through trial-and-error experiments.

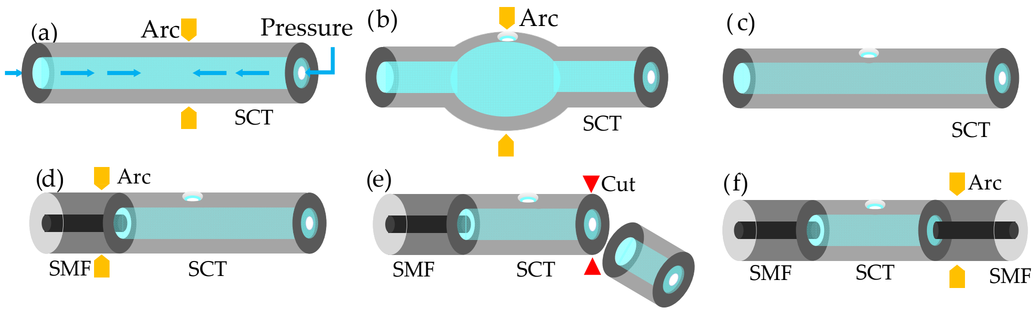

Figure 5. Schematic diagram of the side-hole formation stages. (**a**) SCT in the fusion splicer under pressure. (**b**) First arc discharge expands and tears the SCT creating the bubble. (**c**) Successive arcs stretch the SCT until straight. (**d**) Splicing the SMF with a thick core SCT. (**e**) Cleaving the desired capillary length. (**f**) Splicing the free end of the thick core SCT with an SMF.

Firstly, a long segment of the SCT is placed in the fusion splicer, and one end is glued with UV curable resin to a 0.3 mm PTFE tube connected to a microfluidic electronic pressure sensor from Bartels^{TM} controlled by an Arduino. The other end is glued to a PTFE tube connected to a syringe, whose piston compression increases the pressure in the SCT. Once the desired pressure is achieved, the electric arc discharges can be employed (Figure 5a). The first arc locally heats up the fiber, causing it to expand in the electrode's area. As the expansion persists, the pressure in the capillary causes the fiber to tear up and a bubble appears, creating a micro gas inlet into the capillary (Figure 5b). With each subsequent re-arc, the bubble attains a rounder, more spherical shape, and the fiber stretches and becomes straighter, without strain. This process is repeated until the desired shape is obtained (Figure 5c).

The first method described has been applied in several fiber sensors previously reported; however, the bubble development method has never been employed in an SCT to the best of our knowledge [16,26,27]. Even though Duan et al. have created a microbubble in an SMF via fusion splicing, it worked as an air cavity in the fiber core [28]. The side-hole technique employed by Cordeiro et al. was a proof of concept in PCFs that resulted in high fiber expansion around the hole, and no measurand characterization was performed [17].

Figure 6 shows the microscopic view of several short sensors based on the sandwich configuration. Figure 6a reveals a closed SCT with a length of 609 µm. In Figure 6b, the 645 µm long SCT contains a bubble that acts as an access channel. Its top view is shown in the inset, with an approximate diameter of 45 ± 5 µm. In Figure 6c, the access channel was achieved by splicing a 547 µm long thick-core SCT between an SMF and a thin-core SCT. Sensors with lengths that range from hundreds of microns to a few millimeters were fabricated. It was found that enhanced performances were achieved for the longer sensors, not only towards their spectral results, but also their pressure and temperature responses, particularly due to the creation of better conditions for the AR guidance.

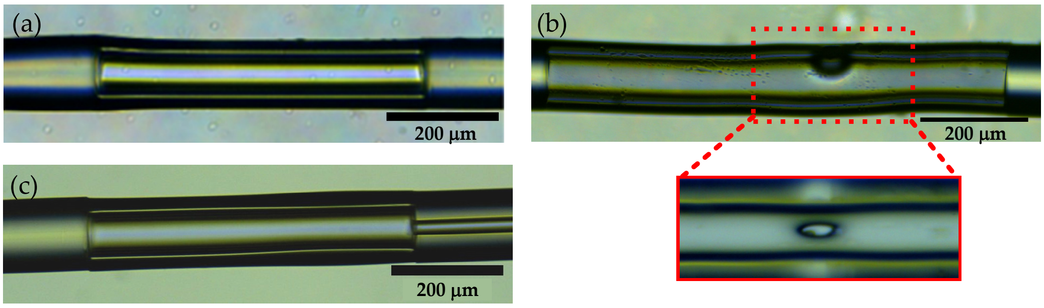

Figure 6. Microscopic view of (**a**) an SMF–SCT–SMF, (**b**) the access channel: a bubble created on the capillary, and (**c**) an SMF–thick-core SCT–thin-core SCT. Inset in (**b**): top view of the bubble.

Spectral analysis was performed in a reflection configuration that is comprised of a broadband light source (BBS) emitting on the C + L band with a wavelength range of 1530–1610 nm. It connects to an optical circulator, which propagates light to the sensor and sends it back to an optical spectrum analyzer (OSA, Anritsu, model MS9740A) with a 0.05 nm resolution. The reflection spectra of the ~2 mm sensors with 0 and 1 access channels (with a bubble or a thin-core SCT) were obtained, as depicted in Figure 7.

Two signals with different oscillation frequencies can be seen simultaneously in the reflection spectrum. The high-frequency oscillation corresponds to the FPI, which is modulated by the AR, a low-frequency oscillation defined by periodic lossy dips. The latter is extracted from the spectrum through usage of an envelope analysis tool, as depicted by the darker upper and lower lines that circumvent the spectrum. This phenomenon arises due to the sensing head length being above critical, corresponding to ~300 µm for the SCT used in this work. The antiresonant peaks should theoretically occur at the same wavelengths when considering the same SCT; however, this is not verified. This is due to deformation of the capillary when instilling the bubble, as well as imperfections in the uniformity along the length of the SCT during its fabrication. Both factors influence the resonance conditions, shifting the AR peak in the spectrum as seen in Figure 7. Additionally, there is a slight AR peak shift between the closed and thin-core SCT sensors, which could be due to the aforementioned uniformity imperfections in the SCT during its fabrication, as well as a possible slight collapse of the thick-core SCT cladding when spliced with the thin-core SCT.

Different amplitudes can be verified in the reflection spectra of the sensors depending on the type of access channel present. The visibility of the reflection spectrum corresponds to $V = \frac{I_M - I_m}{I_M + I_m} \times 100$, where I_M and I_m are the maximum and minimum optical powers of the peak with highest amplitude. The average visibility of closed sensors is 68%, whereas for open sensors it is 26% in thin-core-SCT-based sensors and 45% in bubble-based sensors. Indeed, the highest visibility is observable for the sensors without an access channel, as these elements add perturbances to the waveguides. The lower visibility of the thin-core SCT sensors when compared with the bubble-based sensors is explained by the interface between the SCTs with a thick core and thin core, which results in lower quality mirrors for the FPI when compared with a splice between an SCT and an SMF. Thus, the bubble method showcases a benefit in this regard.

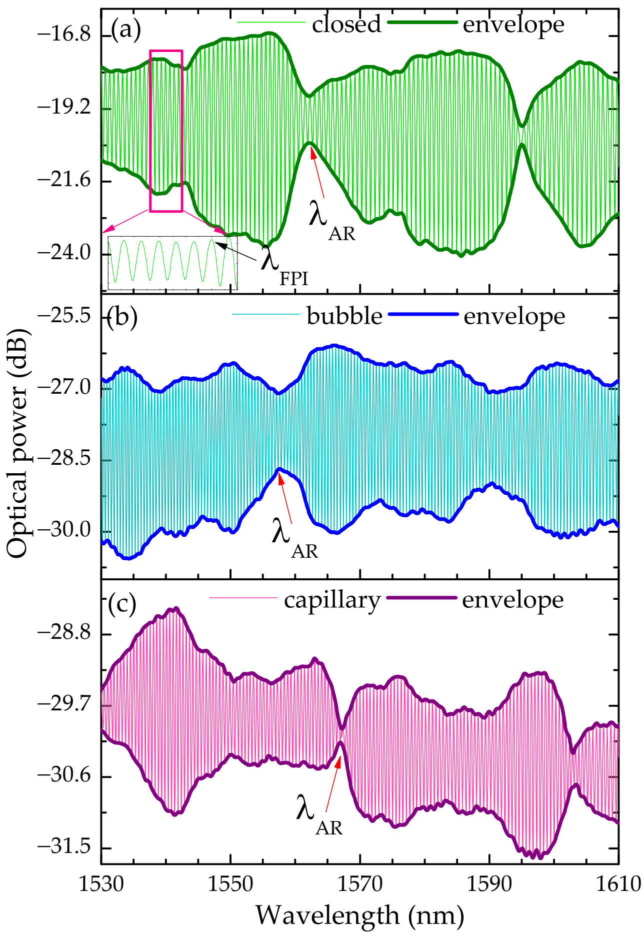

Figure 7. Reflection spectra of the ~2 mm long sensors with (**a**) 0 access channels, (**b**) 1 bubble-based access channel, and (**c**) 1 thin-core-SCT-based access channel. Inset in (**a**): zoom-in in the 1565–1570 nm region.

Similar to the effect evidenced in the FPI visibility, a decrease in this quantity can be seen for the AR spectrum in its low-frequency oscillations given by the envelope of the access-channel-based sensors contrasted against the closed sensors. The introduction of an irregular element in the cladding affects the AR propagation, resulting in an envelope with a lower amplitude, as well as being less shapely than that of a closed sensor.

4. Results and Discussion

The gas-pressure response of the proposed sensor was studied. The sensors monitored this measurand in a closed chamber that was fabricated in-house. The experimental setup, shown in Figure 8, included a chamber with a valve system. One valve was attached to a compressed gas system that enabled air entrance, increasing pressure, while the other allowed the air to escape the chamber, decreasing its pressure. The chamber was connected to an electronic pressure and temperature reading system through the KOLIBRI software desktop.

Pressure measurements between 0 and 0.4 MPa were made at room temperature with steps of 0.05 MPa, wherein the resolution of the electronic pressure sensor is 0.0001 MPa. The sensors used for pressure characterization included closed (without an access channel: FPI_0 and AR_0) and open sensors (with a bubble: FPI_b and AR_b; with a thin-core SCT: FPI_c and AR_c).

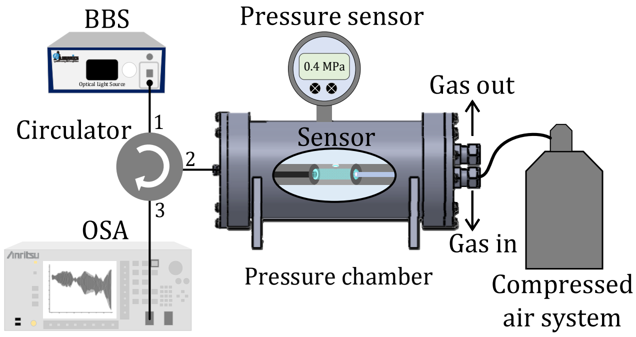

Figure 8. Schematic diagram of the experimental pressure setup.

In Figure 9, it is visible that the closed sensor is insensitive to pressure for both FPI and AR. For open sensors, the FPI showcases a shift towards longer wavelengths (red shift) while the AR component shows a shift towards shorter wavelengths (blue shift). The obtained sensitivities are summarized in Table 1.

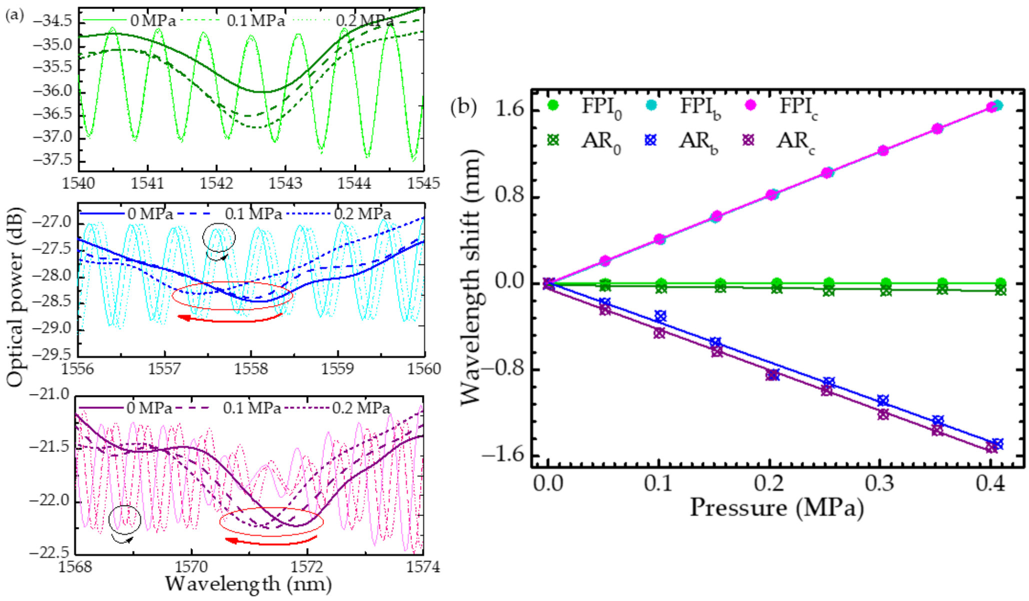

Figure 9. (**a**) Pressure spectra results of the sensors. An offset in the optical power was applied to the AR spectra response for ease of visual perception. The arrows indicate the verified wavelength shift as pressure increases (black for FPI and red for AR). (**b**) Pressure characterization of the sensors.

Table 1. Pressure sensitivities of the sensors.

	κ_{FPI} (nm/MPa)	R^2_{FPI}	κ_{AR} (nm/MPa)	R^2_{AR}
Closed	0.015 ± 0.004	0.6067	-0.13 ± 0.03	0.7103
Bubble	4.085 ± 0.004	0.9999	-3.7 ± 0.1	0.9915
Capillary	4.071 ± 0.005	0.9999	-3.76 ± 0.08	0.9961

It can be seen that the pressure response of the access-channel-based sensors with a bubble vs. a thin-core SCT was found to attain similar results with high linearity, hence validating both access channel methods for pressure detection. The sensitivities obtained experimentally are consistent with the theoretical sensitivities calculated in Section 2, with slight deviations that may be due to the approximations previously considered. This is particularly true for the closed sensor, as the wavelength shift is below the resolution limit, and the linearity achieved is not sufficiently high to determine the sensitivities with precision.

The experimental setup for temperature measurements involved a Peltier cooler and a thermocouple placed on a dissipation block, connected to a temperature controller (Thorlabs (Newton, NJ, USA), TED350) with a resolution of 0.1 °C. The sensors monitored increases in temperature, and increments of 5 °C within the range of 20–80 °C were performed under atmospheric pressure.

It is visible in Figure 10 that the AR underwent a red shift, with much greater sensitivity than that of the FPI. The latter was positive on the closed sensor and negative on the open sensors; however, it is practically insensitive for both configurations. The attained sensitivities are shown in Table 2.

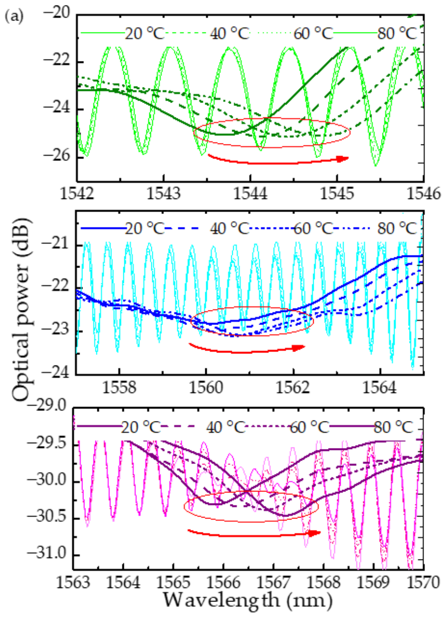

Figure 10. (**a**) Temperature spectra results of the sensors. An offset in the optical power was applied to the AR spectra response for ease of visual perception. The red arrows indicate the verified wavelength shift as temperature increases. (**b**) Temperature characterization of the sensors.

Table 2. Temperature sensitivities of the sensors.

	κ_{FPI} (pm/°C)	R^2_{FPI}	κ_{AR} (pm/°C)	R^2_{AR}
Closed	0.94 ± 0.02	0.9974	18.6 ± 0.4	0.9956
Bubble	−0.20 ± 0.02	0.9108	24.0 ± 0.5	0.9947
Capillary	−0.24 ± 0.04	0.7141	21.8 ± 0.4	0.9964

The deviations evidenced between the theoretical and experimentally attained sensitivities may be caused by the approximations previously considered. Furthermore, the attained results are comparable with those found in the literature [29]. The presence of an access channel might enable the entrance of colder air in the fiber that is outside the influence of the Peltier cooler, whereby the temperature detection results are influenced. A numerical model for describing thermal transport using fractional calculations could be used for the proposed sensor, describing in detail the distribution of temperature in the fiber sensor when using the temperature calibration system for this work [30]. It falls, however, outside of the scope of this work. This issue would possibly be overcome by using a climatic chamber where the entirety of the fiber sensor is under the same temperature environment.

From Table 3, the sensitivities attained for this sensor are comparable with those in the literature. In particular, the FPI and AR sensitivities are within the range of those achieved in previous works, therefore verifying the credibility of the bubble access channel fabrication method.

Table 3. Sensing performance comparison for pressure and temperature measurements.

Structure	Principle	Temperature (pm/°C)	Pressure (nm/MPa)	Simultaneous Measurement	Reference
Air cavity HCF	FPI + AR	584	3.884	Yes	[2]
Collapsed capillary	AR	6.76	4.278	Yes	[3]
Twin-core	MZI	43	−9.6	No	[5]
HC-photonic bandgap fiber	FPI	17,000	1336	Yes	[13]
Thin-core SCT	FPI + AR	0.82 27.7	4.24 −3.76	Yes	[16]
Air cavity microchannel	FPI	7.1	4.028	Yes	[31]
Side hole bubble	FPI + AR	−0.2 24.0	4.085 −3.7	Yes	Our work

When a pressure (ΔP) and temperature (ΔT) variation occurs in the surrounding environment, the reflection spectrum of the sensor will shift accordingly. Considering this shift pertains to a direct linear variation, the wavelength shifts of the FPI and AR can be expressed as:

$$\Delta\lambda_{FPI} = \kappa^{\mathrm{P}}_{FPI}\Delta P + \kappa^{\mathrm{T}}_{FPI}\Delta T, \tag{15}$$

$$\Delta\lambda_{AR} = \kappa^{\mathrm{P}}_{AR}\Delta P + \kappa^{\mathrm{T}}_{AR}\Delta T, \tag{16}$$

where κ_i^j is the sensitivity of the studied interferometer, i (FPI or AR), of the corresponding measurand, j (pressure or temperature). Thus, the total wavelength shift of each interferometer is the sum of the shifts for each measurand. Since the sensitivities of the interferometers were different for both parameters, a hybrid application of the bubble-based sensor can be made for the simultaneous measurement of pressure and temperature by tracing the wavelength shift of each interferometer and solving the following matrix:

$$\begin{bmatrix} \Delta\lambda_{FPI} \\ \Delta\lambda_{AR} \end{bmatrix} = \begin{bmatrix} \kappa^P_{FPI} & \kappa^T_{FPI} \\ \kappa^P_{AR} & \kappa^T_{AR} \end{bmatrix} \begin{bmatrix} \Delta P \\ \Delta T \end{bmatrix}. \tag{17}$$

By calculating the inverse matrix, the variation of pressure and temperature for the bubble- and capillary-based sensors is, therefore, given by:

$$\begin{bmatrix} \Delta P \\ \Delta T \end{bmatrix} = \frac{1}{0.0973} \begin{bmatrix} 0.0240 & 0.00020 \\ 3.7 & 4.085 \end{bmatrix} \begin{bmatrix} \Delta\lambda^b_{FPI} \\ \Delta\lambda^b_{AR} \end{bmatrix}, \tag{18a}$$

$$\begin{bmatrix} \Delta P \\ \Delta T \end{bmatrix} = \frac{1}{0.08785} \begin{bmatrix} 0.0218 & 0.00024 \\ 3.76 & 4.071 \end{bmatrix} \begin{bmatrix} \Delta\lambda^c_{FPI} \\ \Delta\lambda^c_{AR} \end{bmatrix}, \tag{18b}$$

where $D = \kappa^P_{FPI}\kappa^T_{AR} - \kappa^T_{FPI}\kappa^P_{AR}$ is the determinant of the inverse matrix. Note that the units of the sensitivities are in nm/MPa and nm/°C for pressure and temperature, respectively. The resolution measurement of these parameters can be assessed by fixing pressure while varying temperature and keeping temperature fixed whilst changing pressure. Using (18a,b), the ideal and experimentally obtained values of pressure and temperature can be compared.

From Figure 11, a great perpendicularity between both parameters is evident, highlighting a very linear response in the pressure component, whilst the temperature output displays a maximum deviation of ~3 °C, arising from the different orders of magnitude of the pressure and temperature sensitivities. The standard deviation of each parameter gives the resolution of the simultaneous measurements for the sensors, which were calculated to be $\pm 3.01 \times 10^{-4}$ MPa and ± 1.86 °C for pressure and temperature, respectively, for the bubble sensor and $\pm 6.32 \times 10^{-4}$ MPa and ± 1.38 °C for the capillary sensor.

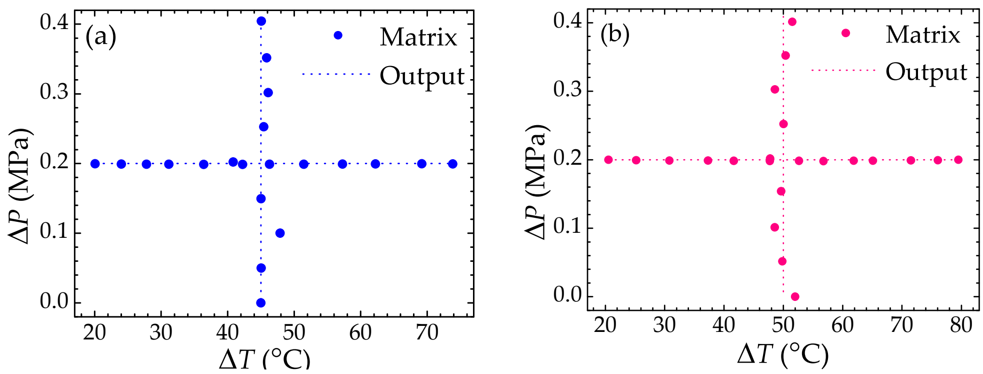

Figure 11. Sensor output of the simultaneous measurement of pressure and temperature for a 2 mm sensor with a (**a**) bubble and a (**b**) thin-core SCT.

Summarizing the performance of the access channel methods, it was found that the spectra amplitude of both the FPI and AR is significantly greater in the bubble-based sensors than the thin-core-based ones. Additionally, similar pressure and temperature sensitivities and resolutions were attained for both methods. The fact that an access channel was achieved in the SCT without substituting any part of the SMF–SCT–SMF configuration grants this structure greater flexibility than the one comprised of a thin-core SCT. On the one hand, the bubble-based sensor is a cheaper configuration than the thin core-SCT method, and the SMF and its length play no part in the working mechanism of the sensor. On the other hand, the bubble-based sensors possess a configuration that can be employed in a transmission scheme, yielding greater versatility in this sensing design contrasted with the thin-core-SCT-based sensors.

5. Conclusions

A hybrid sensor based on a section of SCT with access channels was developed. Two different methods were utilized, involving only a fusion splicer: one was based on splicing the SCT with a thin-core SCT, while the other created a bubble in the SCT, a method that was, to the best of our knowledge, developed for the first time in an SCT for pressure detection. These sensors were studied in a reflection configuration that enhanced FPI and AR phenomena in a single sensing element of a few millimeters. Both interferometers monitored pressure and temperature for closed and open sensors with each method. The different sensitivities of both parameters allowed for a hybrid application of the sensor towards the simultaneous measurement of pressure and temperature. A comparison study between the access channel development methods revealed greater visibility in the FPI and AR spectra of the bubble-based sensors and similar pressure and temperature resolutions for both interferometers when compared with the thin-core-SCT-based sensors. The easy and low-cost fabrication of the access channels, as well as the simple, yet robust structure grant this sensor highly competitive advantages. The convenient reflection probe and the development of up to two access channels potentiate this sensor to be applied in microfluidics by establishing fluid flow from one channel to another.

Author Contributions: J.P.S. performed the experimental and numerical work, collected and analyzed the data, and wrote the manuscript. J.B. and J.K. fabricated the SCT and revised the manuscript. M.S.F. conceived the idea of the study, supervised the experimental work, and contributed to writing and editing the manuscript. All authors have read and agreed to the published version of the manuscript.

Funding: This work was financially supported by the AROMA project, funded by FEDER, through CENTRO2020-Programa Operacional Regional do Centro, CENTRO-01-0145-FEDER-031568, and by national funds (OE) PTDC/EEI-EEE/31568/2017, UIDB/50025/2020, and UIDP/50025/2020, through FCT/MCTES. The work of M. S. Ferreira was supported by CEEC-IND/00777/2018. The work was also funded by the German Federal Ministry of Education and Research (BMBF): "RUBIN—QUANTIFISENS—TP11: Specialty fibers and fiber-based components for omnifunctional fiber sensor systems" (FKZ: 03RU1U071J), as well as the bilateral cooperation of FCT/DAAD (FLOW, Project ID: 57518590).

Institutional Review Board Statement: Not applicable.

Informed Consent Statement: Not applicable.

Data Availability Statement: Not applicable.

Conflicts of Interest: The authors declare no conflict of interest.

References

1. Hou, M.; Zhu, F.; Wang, Y.; Wang, Y.; Liao, C.; Liu, S.; Lu, P. Antiresonant Reflecting Guidance Mechanism in Hollow-Core Fiber for Gas Pressure Sensing. *Opt. Express* **2016**, *24*, 27890–27898. [CrossRef] [PubMed]
2. Gao, H.; Jiang, Y.; Zhang, L.; Cui, Y.; Jiang, Y.; Jia, J.; Jiang, L. Antiresonant Mechanism Based Self-Temperature-Calibrated Fiber Optic Fabry–Perot Gas Pressure Sensors. *Opt. Express* **2019**, *27*, 22181–22189. [CrossRef]
3. Yang, Y.B.; Wang, D.N.; Xu, B.; Wang, Z.K. Optical Fiber Tip Interferometer Gas Pressure Sensor Based on Anti-Resonant Reflecting Guidance Mechanism. *Opt. Fiber Technol.* **2018**, *42*, 11–17. [CrossRef]
4. Zhong, X.; Wang, Y.; Liao, C.; Liu, S.; Tang, J.; Wang, Q. Temperature-Insensitive Gas Pressure Sensor Based on Inflated Long Period Fiber Grating Inscribed in Photonic Crystal Fiber. *Opt. Lett.* **2015**, *40*, 1791–1794. [CrossRef] [PubMed]
5. Li, Z.; Liao, C.; Wang, Y.; Xu, L.; Wang, D.; Dong, X.; Liu, S.; Wang, Q.; Yang, K.; Zhou, J. Highly-Sensitive Gas Pressure Sensor Using Twin-Core Fiber Based in-Line Mach-Zehnder Interferometer. *Opt. Express* **2015**, *23*, 6673–6678. [CrossRef]
6. Fu, H.Y.; Tam, H.Y.; Shao, L.Y.; Dong, X.; Wai, P.K.A.; Lu, C.; Khijwania, S.K. Pressure Sensor Realized with Polarization-Maintaining Photonic Crystal Fiber-Based Sagnac Interferometer. *Appl. Opt.* **2008**, *47*, 2835–2839. [CrossRef]
7. Zhang, Z.; He, J.; Dong, Q.; Bai, Z.; Liao, C.; Wang, Y.; Liu, S.; Guo, K.; Wang, Y. Diaphragm-Free Gas-Pressure Sensor Probe Based on Hollow-Core Photonic Bandgap Fiber. *Opt. Lett.* **2018**, *43*, 3017–3020. [CrossRef]
8. Xu, B.; Wang, C.; Wang, D.N.; Liu, Y.; Li, Y. Fiber-Tip Gas Pressure Sensor Based on Dual Capillaries. *Opt. Express* **2015**, *23*, 23484–23492. [CrossRef]
9. Biswas, U.; Rakshit, J.K.; Suthar, B.; Kumar, D.; Nayak, C. Modeling and Analysis of All-Optical Pressure Sensor Using Photonic Crystal Based Micro Ring Resonator. *Int. J. Numer. Model. Electron. Netw. Devices Fields* **2022**, *35*, e2962. [CrossRef]
10. Patil, P.P.; Kamath, S.P.; Upadhyaya, A.M.; Sharan, P. Design and Analysis of Photonic MEMS Based Micro Ring Resonators for Pressure Sensing Application. *J. Micromech. Microeng.* **2021**, *31*, 115004. [CrossRef]
11. Biswas, U.; Kumar Rakshit, J.; Das, J.; Kumar Bharti, G.; Suthar, B.; Amphawan, A.; Najjar, M. Design of an Ultra-Compact and Highly-Sensitive Temperature Sensor Using Photonic Crystal Based Single Micro-Ring Resonator and Cascaded Micro-Ring Resonator. *Silicon* **2021**, *13*, 885–892. [CrossRef]
12. Pevec, S.; Donlagić, D. Multiparameter Fiber-Optic Sensors: A Review. *Opt. Eng.* **2019**, *58*, 072009. [CrossRef]
13. Zhang, Z.; He, J.; Du, B.; Zhang, F.; Guo, K.; Wang, Y. Measurement of High Pressure and High Temperature Using a Dual-Cavity Fabry–Perot Interferometer Created in Cascade Hollow-Core Fibers. *Opt. Lett.* **2018**, *43*, 6009–6012. [CrossRef] [PubMed]
14. Shao, L.; Liu, Z.; Hu, J.; Gunawardena, D.; Tam, H.Y. Optofluidics in Microstructured Optical Fibers. *Micromachines* **2018**, *9*, 145. [CrossRef] [PubMed]
15. Sloyan, K.; Melkonyan, H.; Apostoleris, H.; Dahlem, M.S.; Chiesa, M.; al Ghaferi, A. A Review of Focused Ion Beam Applications in Optical Fibers. *Nanotechnology* **2021**, *32*, 472004. [CrossRef] [PubMed]
16. He, H.; Liu, Y.; Liao, Y.; Lang, C.; Li, Y.; Qu, S. Simple Fiber-Optic Sensor for Simultaneous and Sensitive Measurement of High Pressure and High Temperature Based on the Silica Capillary Tube. *Opt. Express* **2019**, *27*, 25777–25788. [CrossRef]
17. Cordeiro, C.M.B.; dos Santos, E.M.; Brito Cruz, C.H.; de Matos, C.J.; Ferreira, D.S. Lateral Access to the Holes of Photonic Crystal Fibers—Selective Filling and Sensing Applications. *Opt. Express* **2006**, *14*, 8403–8412. [CrossRef]
18. Malitson, I.H. Interspecimen Comparison of the Refractive Index of Fused Silica. *J. Opt. Soc. Am.* **1965**, *55*, 1205–1209. [CrossRef]
19. Sun, W.; Zhang, X.; Yu, Y.; Yang, L.; Hou, F.; Yang, Y.; Wang, T. Comparative Study on Transmission Mechanisms in a SMF-Capillary-SMF Structure. *J. Light. Technol.* **2020**, *38*, 4075–4085. [CrossRef]
20. Litchinitser, N.M.; Abeeluck, A.K.; Headley, C.; Eggleton, B.J. Antiresonant Reflecting Photonic Crystal Optical Waveguides. *Opt. Lett.* **2002**, *27*, 1592–1594. [CrossRef]
21. Liu, S.; Wang, Y.; Hou, M.; Guo, J.; Li, Z.; Lu, P. Anti-Resonant Reflecting Guidance in Alcohol-Filled Hollow Core Photonic Crystal Fiber for Sensing Applications. *Opt. Express* **2013**, *21*, 31690–31697. [CrossRef]
22. Pang, M.; Xuan, H.F.; Ju, J.; Jin, W. Influence of Strain and Pressure to the Effective Refractive Index of the Fundamental Mode of Hollow-Core Photonic Bandgap Fibers. *Opt. Express* **2010**, *18*, 14041. [CrossRef] [PubMed]

23. Jin, L.; Guan, B.O.; Wei, H. Sensitivity Characteristics of Fabry-Perot Pressure Sensors Based on Hollow-Core Microstructured Fibers. *J. Light. Technol.* **2013**, *31*, 2526–2532. [CrossRef]
24. Cao, Y.; Jin, W.; Yang, F.; Ho, H.L. Phase Sensitivity of Fundamental Mode of Hollow-Core Photonic Bandgap Fiber to Internal Gas Pressure. *Opt. Express* **2014**, *22*, 13190–13201. [CrossRef] [PubMed]
25. Santos, J.L.; Farahi, F. *Handbook of Optical Sensors*; CRC Press: Boca Raton, FL, USA, 2015.
26. Wang, R.; Qiao, X. Hybrid Optical Fiber Fabry–Perot Interferometer for Simultaneous Measurement of Gas Refractive Index and Temperature. *Appl. Opt.* **2014**, *53*, 7724–7728. [CrossRef] [PubMed]
27. Coelho, L.; Tafulo, P.A.R.; Jorge, P.A.S.; Santos, J.L.; Viegas, D.; Schuster, K.; Kobelke, J.; Frazão, O. Simultaneous Measurement of Partial Pressure of O_2 and CO_2 with a Hybrid Interferometer. *Opt. Lett.* **2012**, *37*, 3063–3065. [CrossRef]
28. Duan, D.W.; Rao, Y.J.; Hou, Y.S.; Zhu, T. Microbubble Based Fiber-Optic Fabry-Perot Interferometer Formed by Fusion Splicing Single-Mode Fibers for Strain Measurement. *Appl. Opt.* **2012**, *51*, 1033–1036. [CrossRef]
29. Zhu, C.; Gerald, R.E.; Huang, J. A Dual-Parameter Internally Calibrated Fabry-Perot Microcavity Sensor. *IEEE Sens. J.* **2020**, *20*, 2511–2517. [CrossRef]
30. Hernández-Acosta, M.A.; Martines-Arano, H.; Soto-Ruvalcaba, L.; Martínez-González, C.L.; Martínez-Gutiérrez, H.; Torres-Torres, C. Fractional Thermal Transport and Twisted Light Induced by an Optical Two-Wave Mixing in Single-Wall Carbon Nanotubes. *Int. J. Therm. Sci.* **2020**, *147*, 106136. [CrossRef]
31. Xu, B.; Liu, Y.; Wang, D.; Jia, D.; Jiang, C. Optical Fiber Fabry-Pérot Interferometer Based on an Air Cavity for Gas Pressure Sensing. *IEEE Photonics J.* **2017**, *9*, 7102309. [CrossRef]